Resolution enhancement in standing-wave total internal reflection microscopy: a point-spread-function engineering approach

Peter T. C. So, Hyuk-Sang Kwon, and Chen Y. Dong

Department of Mechanical Engineering, Massachusetts Institute of Technology, Cambridge, Massachusetts 02139

Received December 22, 2000; revised manuscript received April 3, 2001; accepted April 17, 2001

The theoretical basis for resolution enhancement in standing-wave total internal reflection microscopy (SW-TIRM) is examined. This technique relies on the formation of an excitation field containing super-diffraction-limited spatial-frequency components. Although the fluorescence generated at the object planes contains high-frequency information of the object distribution, this information is lost at the image plane, where the detection optics acts as a low-pass filter. From the perspective of point-spread-function (PSF) engineering, one can show that if this excitation field is translatable experimentally, the high-frequency information can be extracted from a set of images where the excitation fields have different displacement vectors. We have developed algorithms to combine this image set to generate a composite image with an effective PSF that is equal to the product of the excitation field and the Fraunhofer PSF. This approach can easily be extended to incorporate nonlinear excitation modalities into SW-TIRM for further resolution improvement. We theoretically examine high-resolution imaging based on the addition of two-photon, pump–probe, and stimulated-emission depletion methods to SW-TIRM and show that resolution better than 1/20 of the emission wavelength may be achievable.

OCIS codes: 180.0180, 180.2520, 260.6970, 190.4180.

1. INTRODUCTION

Light microscopy is widely used in biomedical research to study living biological systems. A major limitation of optical imaging is its inability to resolve objects with separation below several hundred nanometers. Today, electron microscopy is one of the few ways to image biomedical specimens on the nanometer scale. Although electron microscopy is a powerful high-resolution imaging technique, it is restricted to the study of fixed specimens. A number of scanning-probe methods have also been developed to circumvent this limitation, including scanning tunneling microscopy, atomic-force microscopy and near-field optical microscopy.[1–3] Unfortunately, while scanning-probe microscopic techniques have achieved atomic resolution in solid-state samples, there is significant resolution degradation in soft biological specimens. For example, while near-field optical microscopy can, in principle, achieve resolution that is on the order of 10 nm (Ref. 3), the practical resolution achieved in a biological specimen is often on the range of 50–100 nm (Refs. 4–6). In biological specimens, the application of scanning-probe techniques further suffers from slow imaging speed, the confinement to two dimensions, and the undesirable mechanical contact with the specimen. There is a need to develop a completely optical imaging method with better than 100-nm resolution.

The imaging resolution of microscopy imaging is limited by the Fraunhofer diffraction of light. The well-known Abbe limit codifies the relationship between lateral resolution (Δr) with the wavelength of the emission (λ_e) and the numerical aperture of the imaging optics (NA). By the Rayleigh criterion, the resolution of conventional microscopy is given by the FWHM of its point-spread function (PSF), $\Delta r \approx \lambda_e/2\mathrm{NA}$. A number of coherent excitation and detection techniques such as confocal[7–10] and 4-π microscopy[11–14] with use of high-numerical-aperture objectives provides depth discrimination and allows three-dimensional (3-D) imaging. However, the improvement in lateral direction is modest, and the typical resolution is $\Delta r \approx \lambda_e/3$ for high-numerical-aperture objectives ($\mathrm{NA} \approx 1$). Another approach to improve optical microscopy resolution involves the use of nonlinear optical excitation. Most nonlinear methods such as two-photon[15–17] and pump–probe microscopy[18–20] also provide three-dimensional (3-D) depth discrimination but only very modest improvement in the lateral dimension. The most promising nonlinear excitation technique for lateral resolution improvement is stimulated-emission depletion (STED) microscopy.[21–23] By driving the fluorescence signal to response nonlinearly to the excitation signal, this technique has achieved a fivefold resolution improvement in axial direction and over twofold improvement in the lateral direction.

Another promising way to improve microscopy resolution involves the use of standing-wave excitation.[24,25] Standing-wave optical microscopy was first developed to provide fast, 3-D-resolved wide-field imaging with an axial resolution of $\lambda_e/4$ (Refs. 26 and 27). In this implementation, there is no lateral resolution enhancement. The use of standing-wave imaging in a total internal reflection and other geometry have shown that lateral resolution better than $\lambda_e/7$ can be achieved.[28] This resolution

is comparable or better than near-field optical scanning microscopy and atomic-force microscopy in many biological specimens.

Although resolution improvement based on the formation of standing waves has been used for over a decade, a number of theoretical issues remain to be explored. In this paper, we will examine algorithms that allow the generation of an improved final image containing the same spatial-frequency content of the excitation light field. We will show that these algorithms are not specific to the SW-TIRM problem but are valid for a broad range of imaging problems when there is a spatially translatable excitation field containing super-diffraction-limited frequencies (a super-diffraction-limited excitation field is defined as an optical field containing spatial frequencies higher than NA/λ_e). These theoretical results are used to explore the potential for further resolution enhancement in SW-TIRM by incorporating nonlinear processes such as multiphoton, pump–probe, and STED excitations. Finally, this paper considers only fluorescence SW-TIRM under incoherent imaging condition. While SW-TIRM may possibly work in reflected (scattered) light mode, this case will not be considered because of greatly increased difficulties in treating coherent imaging cases.

2. RESOLUTION ENHANCEMENT BASED ON SUPER-DIFFRACTION-LIMITED EXCITATION FIELD

The image-formation process in a fluorescent microscope can be readily formulated mathematically. Let $O(\mathbf{r})$ be the distribution of fluorescent objects, the concentration distribution of fluorophores. Let $E(\mathbf{r})$ be the excitation field, the intensity distribution of the excitation light. The position vector $\mathbf{r}$ is a two-dimensional vector on the object plane. With no loss of generality, the magnification of the microscope can be assumed to be unity. In this case, the position vector on the object plane also characterizes the positions on the image plane. Let $I(\mathbf{r})$ be the signal-intensity distribution on the image plane.

Let $P(\mathbf{r})$ be the objective emission point-spread function (PSF) based on the Fraunhofer approximation,

$$P(\mathbf{r}) = \left[\frac{2J_1(2\pi \mathrm{NA}|\mathbf{r}|/\lambda_e)}{2\pi \mathrm{NA}|\mathbf{r}|/\lambda_e}\right]^2, \tag{1}$$

where J_1 is the first-order Bessel function and NA is the numerical aperture of the objective.

In this case, the image function of a microscope can be expressed as

$$I(\mathbf{r}) = [O(\mathbf{r})E(\mathbf{r})] \otimes P(\mathbf{r}), \tag{2}$$

where $\otimes$ denotes a convolution operation. If $E(\mathbf{r})$ is uniform, this expression represents the case of standard wide-field fluorescence microscopy imaging.

The excitation field $E(\mathbf{r})$ is assumed to possess two properties. First, $E(\mathbf{r})$ is translatable; its placement on the object plane can be experimentally controlled. Second, $E(\mathbf{r})$ contains higher spatial frequencies than the Fraunhofer PSF.

With the first assumption, Eq. (2) can be written more generally as

$$I(\mathbf{r},\mathbf{r}') = [O(\mathbf{r})E(\mathbf{r} - \mathbf{r}')] \otimes P(\mathbf{r}), \tag{3}$$

where $\mathbf{r}'$ is a position vector on the object plane that measures the translation of the excitation light profile relative to an arbitrary origin.

For clarity, we will restrict our discussions to one dimension. The basic method for extending the one-dimensional case to higher dimensions has been discussed in previous publications.[24,25] A more in-depth theoretical examination of this extension will be covered in the future. Replacing positional variables $\mathbf{r}$ and $\mathbf{r}'$ with x and x', we can write Eq. (3) as

$$I(x, x') = [O(x)E(x - x')] \otimes P(x). \tag{4}$$

Computationally, one can always synthesize a new image $I'(x)$ as a weighted sum of images recorded at a set of translation shift vectors $\{x'\}$,

$$I'(x) = \sum_{\{x'\}} f(x, x')I(x, x'), \tag{5}$$

where $f(x, x')$ is an arbitrary weighting function. In the following discussions, we refer to $I'(x)$ as the composite image and the set of images, $I(x, x')$, as the intermediate images.

Expanding the convolution integral explicitly, one obtains

$$I'(x) = \sum_{\{x'\}} f(x, x') \int_{-\infty}^{\infty} O(x'')E(x'' - x')P(x - x'')\mathrm{d}x''. \tag{6}$$

After exchanging the order of the integral and the summation,

$$I'(x) = \int_{-\infty}^{\infty} O(x'')\left[\sum_{\{x'\}} f(x, x')E(x'' - x')\right]P(x - x'')\mathrm{d}x''. \tag{7}$$

If $\{x'\}$ and $f(x, x')$ satisfy the following equation:

$$\sum_{\{x'\}} f(x, x')E(x'' - x') = E(x - x''), \tag{8}$$

Equation (7) can be rewritten as

$$I'(x) = \int_{-\infty}^{\infty} O(x'')E(x - x'')P(x - x'')\mathrm{d}x''. \tag{9}$$

This gives

$$I'(x) = O(x) \otimes [E(x)P(x)]. \tag{10}$$

The new image $I'(x)$ is the convolution of the object function with an effective PSF, $E(x)P(x)$. From the second assumption about the excitation field, this PSF containing super-diffraction-limited frequency components originated from $E(x)$; the composite image has higher resolution than the intermediate images. The task of generating a composite image with super-diffraction-limited resolution reduces to finding a set of shift vectors $\{x'\}$ and a weighting function $f(x, x')$ that satisfies Eq. (8). We will consider two approaches to accomplish this task. The first algorithm will be based on Fourier decomposition of $f(x, x')$, and the second algorithm will be based on impulse-function decomposition.

3. RESOLUTION ENHANCEMENT BASED ON FOURIER DECOMPOSITION

An excitation profile with known functional form can always be expanded as a Fourier series. Consider a Fourier expansion of $E(x)$:

$$E(x) = \sum_{n=0}^{\infty} a_n \cos(nkx) + b_n \sin(nkx). \tag{11}$$

Equation (8) can be written as

$$\sum_{\{x'\}} \sum_{n=0}^{\infty} f(x, x')\{a_n \cos[nk(x'' - x')] + b_n \sin[nk(x'' - x')]\} = \sum_{n=0}^{\infty} a_n \cos[nk(x - x'')] + b_n \sin[nk(x - x'')]. \tag{12}$$

The right-hand side of Eq. (12) can be written as

$$\begin{aligned}\sum_{n=0}^{\infty} a_n \cos[nk(x - x'')] + b_n \sin[nk(x - x'')] &= a_0 + [a_1 \cos(kx) + b_1 \sin(kx)]\cos(kx'') \\ &+ [a_1 \sin(kx) - b_1 \cos(kx)]\sin(kx'') + \ldots \\ &+ [a_n \cos(nkx) + b_n \sin(nkx)]\cos(nkx'') \\ &+ [a_n \sin(nkx) - b_n \cos(nkx)]\sin(nkx'') + \cdots.\end{aligned} \tag{13}$$

The left-hand side of Eq. (12) can be written as

$$\begin{aligned}\sum_{\{x'\}} \sum_{n=0}^{\infty} f(x, x')\{a_n \cos[nk(x'' - x')] + b_n \sin[nk(x'' - x')]\} &= a_0 \sum_{\{x'\}} f(x, x') + \sum_{\{x'\}} f(x, x')[a_1 \cos(kx') - b_1 \sin(kx')]\cos(kx'') \\ &+ \sum_{\{x'\}} f(x, x')[a_1 \sin(kx') + b_1 \cos(kx')]\sin(kx'') + \cdots \\ &+ \sum_{\{x'\}} f(x, x')[a_n \cos(nkx') - b_n \sin(nkx')]\cos(nkx'') \\ &+ \sum_{\{x'\}} f(x, x')[a_n \sin(nkx') + b_n \cos(nkx')]\sin(nkx'') + \cdots.\end{aligned} \tag{14}$$

Since x'' is an independent variable, the coefficients for each $\cos(nkx'')$ and $\sin(nkx'')$ terms must be equal. A system of equations is obtained:

$$\begin{aligned}&\sum_{\{x'\}} f(x, x') = 1, \\ &\sum_{\{x'\}} f(x, x')[a_1 \cos(kx') - b_1 \sin(kx')] = a_1 \cos(kx) + b_1 \sin(kx), \\ &\sum_{\{x'\}} f(x, x')[a_1 \sin(kx') + b_1 \cos(kx')] = a_1 \sin(kx) - b_1 \cos(kx) \\ &\vdots \\ &\sum_{\{x'\}} f(x, x')[a_n \cos(nkx') - b_n \sin(nkx')] = a_n \cos(nkx) + b_n \sin(nkx), \\ &\sum_{\{x'\}} f(x, x')[a_n \sin(nkx') + b_n \cos(nkx')] = a_n \sin(nkx) - b_n \cos(nkx) \\ &\vdots\end{aligned} \tag{15}$$

Let m be the index of the highest order of nonzero Fourier component in the expansion of $E(x)$. Equation (15) is a system of $2m + 1$ equations. Since the set of vectors $Y = \{1, \cos(kx), \sin(kx), \ldots, \cos(nkx), \sin(nkx), \ldots\}$ is independent and complete, $f(x, x')$ can be expanded in terms of them:

$$f(x, x') = A_0(x') + A_1(x')\cos(kx) + B_1(x')\sin(kx) + \cdots + A_n(x')\cos(nkx) + B_n(x')\sin(nkx) + \cdots. \tag{16}$$

We can terminate the expansion at order m, as there are no higher-frequency components in this problem. After substituting Eq. (16) into Eq. (15), each equation in the system [Eq. (15)] can be rewritten as $2m + 1$ independent equations because of the orthogonality of the elements in Y. Therefore, Eq. (15) actually represents a system of $(2m + 1) \times (2m + 1)$ independent equations.

To ensure that Eq. (15) can be solved, the set of shift vectors, $\{x'\}$, must contain enough independent variables. For each new element x_i in the set $\{x'\}$, we introduce $2m + 2$ independent variables, including $2m + 1$ coefficients of $f(x, x')$: $A_0(x_i)$, $A_1(x_i)$, $B_1(x_i), \ldots, A_m(x_i)$, $B_m(x_i)$, and the shift vector itself, x_i. This implies that at least $2m + 1$ elements are needed in this set of shift vectors to keep this system of equations from being overdetermined. However, the system is under-determined with $2m + 1$ shift elements in the set. Among the $(2m + 2) \times (2m + 1)$ variables, $2m + 1$ of these variables can be chosen arbitrarily. Experimentally, these $2m + 1$ variables are typically taken to be the shift vectors of the excitation field.

Let $\{x_0, x_1, \ldots, x_{2m}\}$ be the set of chosen shift vectors, and simplifying notations by introducing variables $A_{00} = A_0(x_0)$, $A_{01} = A_0(x_1)$, $B_{01} = B_0(x_1)$, $A_{10} = A_1(x_0)$, $B_{10} = B_1(x_0)$, etc., Eq. (15) can be expressed compactly in matrix form:

$$\begin{bmatrix} 1 & \cdots & 1 \\ a_1\cos(kx_0) - b_1\sin(kx_0) & \cdots & a_1\cos(kx_{2m}) - b_1\sin(kx_{2m}) \\ a_1\sin(kx_0) + b_1\cos(kx_0) & \cdots & a_1\sin(kx_{2m}) + b_1\cos(kx_{2m}) \\ \vdots & \ddots & \vdots \\ a_m\cos(mkx_0) - b_m\sin(mkx_0) & \cdots & a_m\cos(mkx_{2m}) - b_m\sin(mkx_{2m}) \\ a_m\sin(mkx_0) + b_m\cos(mkx_0) & \cdots & a_m\sin(mkx_{2m}) + b_m\cos(mkx_{2m}) \end{bmatrix}$$

$$\times \begin{bmatrix} A_{00} & A_{10} & B_{10} & \cdots & A_{m,0} & B_{m,0} \\ A_{01} & A_{11} & B_{11} & \cdots & A_{m,1} & B_{m,1} \\ \vdots & \vdots & \vdots & \ddots & \vdots & \vdots \\ A_{0,2m} & A_{1,2m} & B_{1,2,m} & \cdots & A_{m,2m} & B_{m,2m} \end{bmatrix} = \begin{bmatrix} 1 & & & & & \\ & a_1 & b_1 & & 0 & \\ & -b_1 & a_1 & & & \\ & & & \ddots & & \\ & 0 & & & a_m & b_m \\ & & & & -b_m & a_m \end{bmatrix}. \quad (17)$$

Each of these are a $2m + 1 \times 2m + 1$ square matrix. The first matrix, S, contains the shift vectors and the Fourier components of the excitation field; the second matrix, A, contains the unknown variables of $f(x, x')$ that specify this weighting function; the rightmost matrix, E, contains Fourier components' information of the excitation profile.

After redefining terms, this equation can be rewritten as

$$S \times A = E. \quad (18)$$

This equation is solvable if S is nonsingular, i.e.,

$$\det(S) \neq 0, \quad (19)$$

where det() is the determinant function.

For a nonsingular matrix S, its left inverse S^{-1} exists such that

$$S^{-1}S = I, \quad (20)$$

where I is the identity matrix.

The unknown matrix A can be then be solved as

$$A = S^{-1}E. \quad (21)$$

Therefore $f(x, x')$ is determined through the calculation of the inverse of S.

The choice of shift vectors requires further discussion. We have shown that for an excitation field with the highest-order component being m, at least $2m + 1$ shift vectors are needed. This requirement can also be seen from Eq. (19); if any two shift vectors are equal, matrix S will contain two identical columns, and its determinant vanishes. In addition to being distinct, algebra imposes no further constraints on the choice of the shift vectors. Although mathematics alone does not dictate the choice of shift vectors, a poor choice will compromise final image S/N level. In the absence of *a priori* knowledge of fluorophore distribution on the object plane, the shift vectors should be chosen such that each location on the object plane receives an approximately equal dose of light. The effect of shift-vector choices will be further examined in the following sections.

We will further consider a commonly occurring case where the excitation profile is an even function, i.e. $b_n = 0$ for all n. The matrix equation [Eq. (17)] can be further simplified. Matrix S is reduced to

$$S = \begin{bmatrix} 1 & \cdots & 1 \\ \cos(kx_0) & \cdots & \cos(kx_{2m}) \\ \sin(kx_0) & \cdots & \sin(kx_{2m}) \\ \vdots & \ddots & \vdots \\ \cos(mkx_0) & \cdots & \cos(mkx_{2m}) \\ \sin(mkx_0) & \cdots & \sin(mkx_{2m}) \end{bmatrix}, \quad (22)$$

and matrix E reduces to the identity matrix I.

Therefore in the presence of an excitation field with even symmetry the solution matrix A has a very simple form:

$$A = S^{-1}. \quad (23)$$

A. Standing-Wave Total Internal Reflection Microscopy

SW-TIRM is an exciting new method for high-resolution imaging based on the generation of an excitation field with super-diffraction-limited spatial frequencies. This excitation field is generated through establishment of a standing evanescence wave at the surface of a high-refractive-index substrate on the basis of interference. This standing-wave field has wavelength a factor of $2n$ less than that of light in free space, where n is the index of refraction of the substrate. The index of refraction can be as high as 1.9 for quartz and over 3 for semiconductor materials. Standing evanescence wave fields can obtain spatial frequencies 4–6 times higher than is achievable through use of traditional diffraction-limited optics. The theory and application of SW-TIRM for super-diffraction-limited imaging has been previously discussed,[24] but not in the general context of PSF engineering. In this section, we will examine the resolution of SW-TIRM from the perspective of PSF engineering. For SW-TIRM, the excitation profile can be expanded as a Fourier series of only two terms:

$$E(x) = 1 + \cos(Kx). \quad (24)$$

The spatial wave number is

$$K = 4\pi n \sin(\theta)/\lambda, \quad (25)$$

where n is the index of refraction of the substrate, θ is the incident angle of the light, and λ is the wavelength of the excitation light. The relevant Fourier components are

$a_0 = 1$, $a_1 = 1$. All higher-order a_n and b_n are zero. The highest index of the Fourier components, m, is 1.

In this case, $f(x, x')$ can be expanded in terms of a set of orthogonal vectors: $\{1, \cos Kx, \sin Kx\}$:

$$f(x, x') = A_0(x') + A_1(x')\cos Kx + A_2(x')\sin Kx. \quad (26)$$

Since the highest index of the Fourier component is one, we will need three shift vectors in $\{x'\} = \{x_0, x_1, x_2\}$.

Matrix S can be written as

$$S = \begin{bmatrix} 1 & 1 & 1 \\ \cos Kx_0 & \cos Kx_1 & \cos Kx_2 \\ \sin Kx_0 & \sin Kx_1 & \sin Kx_2 \end{bmatrix}. \quad (27)$$

From the periodicity of these equations, the element in the set needs to span only a range of $0-2\pi/K$. We will choose a set of shift vectors that equally spans this range:

$$\{x'\} = \left\{0, \frac{2\pi}{3}, -\frac{2\pi}{3}\right\} \quad (28)$$

Therefore

$$S = \begin{bmatrix} 1 & 1 & 1 \\ 1 & -1/2 & -1/2 \\ 0 & \sqrt{3}/2 & -\sqrt{3}/2 \end{bmatrix}. \quad (29)$$

The determinant of this matrix is nonzero, and the inverse of the matrix can be readily calculated:

$$A = S^{-1} = \begin{bmatrix} 1/3 & 2/3 & 0 \\ 1/3 & -1/3 & \sqrt{3}/3 \\ 1/3 & -1/3 & -\sqrt{3}/3 \end{bmatrix}. \quad (30)$$

The specification of the set of shift vectors and the associated weighting function [Eqs. (26), (28), and (30)] completely determines the algorithm for constructing a high-resolution composite image in the SW-TIRM setting. This algorithm will be evaluated on the basis of numerically simulated composite images generated from two object functions:

$$O_1(x) = \begin{cases} 1 & \text{if } |x| < 1 \text{ nm} \\ 0 & \text{elsewhere} \end{cases}, \quad (31)$$

$$O_2(x, a) = \begin{cases} 1 & a < x < a + 2 \text{ nm} \\ 1 & -a - 2 \text{ nm} < x < -a \\ 0 & \text{elsewhere} \end{cases}. \quad (32)$$

The object function $O_1(x)$ represents an effective point source centered at the origin. The fluorescence image generated from this object function is the PSF. For any arbitrary extended object function, the fluorescence image can be calculated by convoluting the object function with the PSF as described by Eq. (2). The object function $O_2(x, a)$ represents two point sources separated by a distance of $2a$.

For the simulations in this report, we use parameters that are experimentally realizable. The refractive index of the high-index quartz substrate, n, is assumed to be 1.75. The refractive index of the specimen, n_w, is assumed to be 1.33 (index of water). The wavelengths of the excitation and the emission light are assumed to be 450 and 510 nm, respectively. The incident angle of the excitation light up on the substrate is chosen to be 75°. The signal will be detected by an objective with numerical aperture NA equal to 1.6.

Using the algorithm specified by Eqs. (5), (26), (28), and (30), we can numerically simulate the composite image generated from the point-source object function $O_1(x)$. The result represents the effective PSF of the composite image [Fig. 1(a)]. This PSF is identical to the product of the Fraunhofer PSF with the high-frequency excitation field, as predicted by Eq. (10). To demonstrate resolution improvement based on SW-TIRM method, we have also plotted the conventional diffraction-limited PSF [Fig. 1(a)]. In comparison, we can see that the SW-TIRM offers a PSF with a FWHM that is almost a factor of three narrower than the conventional method. The modulation transfer functions (MTFs) of these PSFs can be readily calculated and are presented in Fig. 1(b).

Using SW-TIRM, we present the composite images of two point objects at different separation distances, $O_2(x)$, in Fig. 2(a). We also simulated composite images based on the same object functions by using a conventional fluorescence microscope [Fig. 2(b)]. We can see that SW-TIRM is capable of resolving objects separated by about 60–70 nm based on the Rayleigh criterion.

The issue of shift-vector choice can be further investigated. Assuming that photon shot noise is the dominant

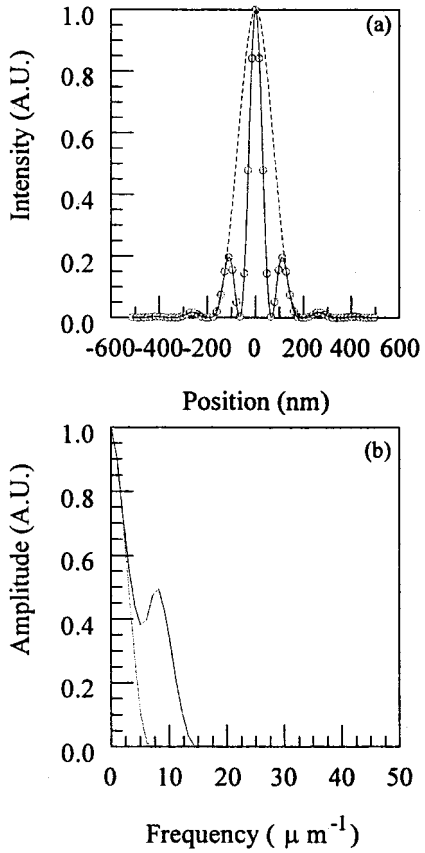

Fig. 1. (a) Franhoffer diffraction-limited PSF (dotted curves), the SW-TIRM PSF predicted by Eq. (10) (solid curves), and the composite image of a point source generated by numerical simulation (data points). (b) Franhoffer diffraction-limited MTF (dotted curves), and the SW-TIRM MTF (solid curves).

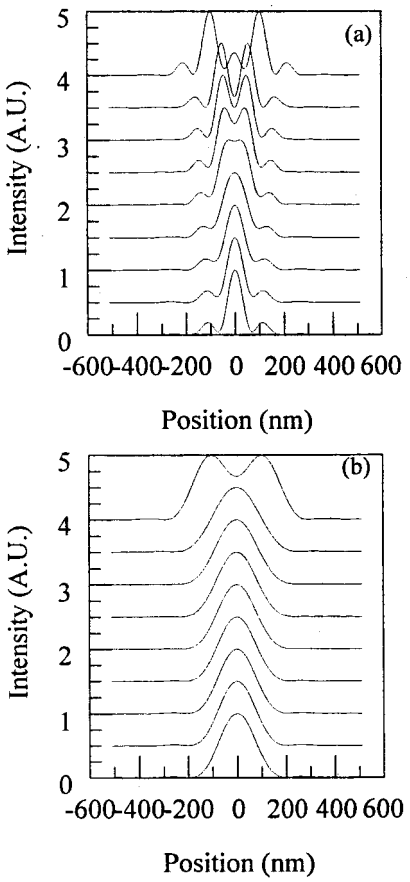

Fig. 2. (a) Simulated composite images for SW-TIRM imaging of two point objects separated by 20, 30, 40, 50, 60, 70, 80, 100, and 200 nm. (b) Simulated composite images for conventional fluorescence microscopic imaging of two point objects separated by 20, 30, 40, 50, 60, 70, 80, 100, and 200 nm. These images are normalized and are displaced from each other vertically for the clarity of the presentation.

noise source in each of the intermediate images, the noise amplitude distribution in the final image can be calculated as[29]

$$N(x) = \left[\sum_{\{x'\}} I(x, x')f(x, x')^2\right]^{1/2}. \tag{33}$$

This gives signal-to-noise (S/N) ratio distribution as

$$\mathrm{S/N}(x) = \frac{I'(x)}{N(x)}. \tag{34}$$

The effect of S/N as a function of shift-vector choice will be investigated with use of an object function,

$$O_3(x) = O_0, \tag{35}$$

where O_0 is a constant. This object function represents a uniform fluorophore distribution on the object plane. We found that the final composite image $I'(x)$ is approximately independent of shift-vector choice as expected. The S/N distributions, $S/N(x)$, are presented in Fig. 3 with use of different sets of shift vectors. We can see that the noise is minimized in the composite image if the shift vectors equally span the period of the lowest nonzero frequency component of the excitation field [Fig. 3(a)]. This is the choice that was made in the preceding discussions. It can be shown that this condition corresponds to maximizing $\det(S)$. As the shift vectors become more clustered [Figs. 3(b)–3(f)], they span a narrower phase space. There is a steady degradation of S/N level at the regions of the object plane that fall outside the maxima of the excitation field [Figs. 3(b)–3(f)]. Note that while a lower S/N level reduces image information content, the resolution of an image is not directly affected as long as S/N level remains above unity. Furthermore, the choosing of equally spaced shift vectors optimizes the S/N level only for a uniform fluorophore distribution. However, this choice is also appropriate for the case that the fluorophore distribution is unknown.

B. Two-Photon Standing-Wave Total Internal Reflection Microscopy

Two-photon excitation is a promising direction for improving SW-TIRM images. The algorithm described in Sub-

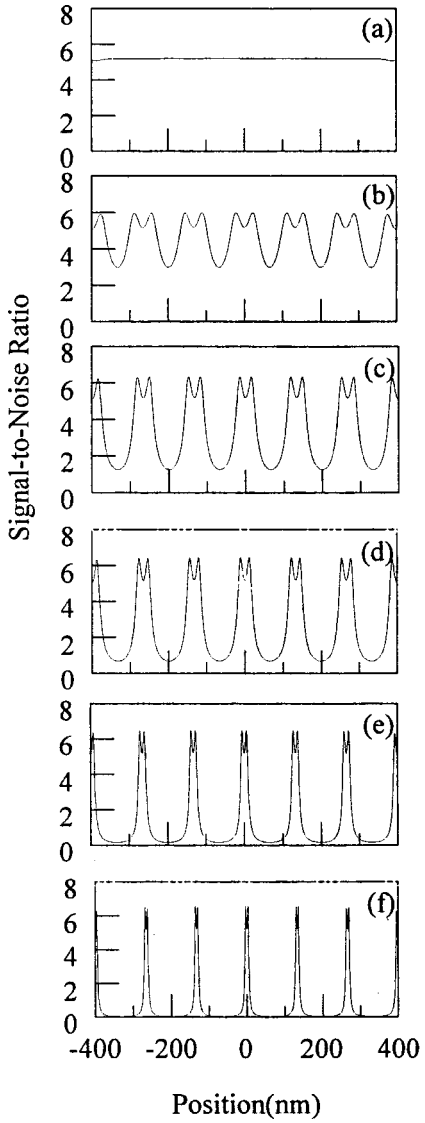

Fig. 3. The S/N distribution in reconstructed SW-TIRM images for different shift-vector choices: (a) $\{x'\} = \{0, 2\pi/3, -2\pi/3\}$, (b) $\{x'\} = \{0, \pi/2, -\pi/2\}$, (c) $\{x'\} = \{0, \pi/3, -\pi/3\}$, (d) $\{x'\} = \{0, \pi/4, -\pi/4\}$, (d) $\{x'\} = \{0, \pi/8, -\pi/8\}$, (e) $\{x'\} = \{0, \pi/16, -\pi/16\}$.

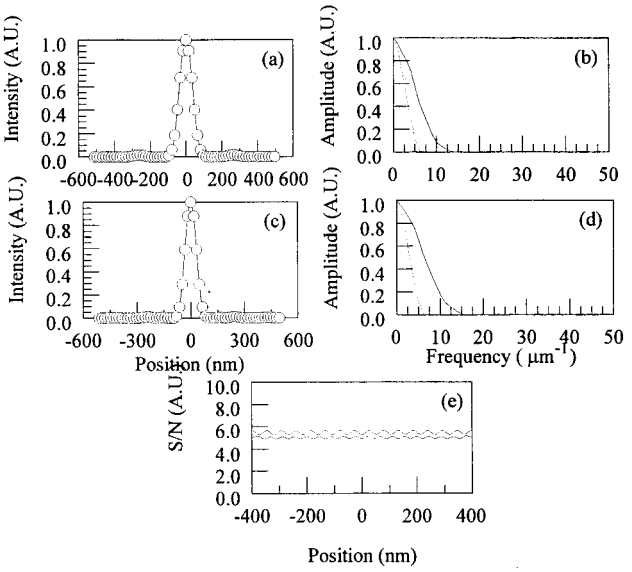

Fig. 4. (a) Theoretical PSF of two-photon SW-TIRM at 900-nm excitation as predicted by Eq. (10) (solid curves) and simulated composite image of a point source imaged by two-photon SW-TIRM at 900 nm (data points). (b) MTF of two-photon SW-TIRM with 900-nm excitation (solid curves) and MTF of Fraunhofer diffraction PSF (dotted curves). (c) Theoretical PSF of two-photon SW-TIRM at 750-nm excitation as predicted by Eq. (10) (solid curves) and simulated composite image of a point source imaged by two-photon SW-TIRM at 750 nm (data points). (d) MTF of two-photon SW-TIRM with 750-nm excitation (solid curves) and MTF of Fraunhofer diffraction PSF (dotted curves). (e) S/N distribution in two-photon SW-TIRM images with excitation wavelength at 750 nm (upper curve) and at 900 nm (lower curve).

section 3.A can be extended to cover the two-photon case. For two-photon, the fluorescence signal is a quadratic function of the excitation field. Equation (13) is modified as

$$E_{2p}(x) = E(x)^2 = \frac{1}{4}[1 + \cos(Kx)]^2$$

$$= \frac{3}{8} + \frac{1}{2}\cos(Kx) + \frac{1}{8}\cos(2Kx). \qquad (36)$$

Note that two-photon excitation of a given fluorophore typically requires an excitation wavelength that is approximately twice that of the one-photon case; hence, the wave vector K is about half of the standard SW-TIRM case.

The excitation profile for two-photon excitation is even with $a_0 = 3/8$, $a_1 = 1/2$, and $a_2 = 1/8$. All higher-order a_n and all b_n are zero. We can expand $f(x, x')$ in terms of the relevant basis vectors:

$$f(x, x') = A_0(x') + A_1(x')\cos Kx + A_2(x')\sin Kx$$

$$+ A_3(x')\cos 2Kx + A_4(x')\sin 2Kx. \qquad (37)$$

Since the highest order of the Fourier component is 2, the set of shift vectors must contain at least five distinct elements:

$$\{x'\} = \left\{0, \frac{2\pi}{5K}, -\frac{2\pi}{5K}, \frac{4\pi}{5K}, -\frac{4\pi}{5K}\right\}. \qquad (38)$$

The matrix A for two-photon excitation can be evaluated to be

$$A = \begin{bmatrix} 0.2 & 0.4 & 0 & 0.4 & 0 \\ 0.2 & 0.124 & 0.38 & -0.324 & 0.235 \\ 0.2 & 0.124 & -0.38 & -0.324 & -0.235 \\ 0.2 & -0.324 & 0.235 & 0.124 & -0.38 \\ 0.2 & -0.324 & -0.235 & 0.124 & 0.38 \end{bmatrix}. \qquad (39)$$

For numerical simulation, we choose an excitation wavelength of 900 nm that is twice the one-photon case value while keeping all other parameters constant. The expected PSF for the two-photon SW-TIRM, as predicted by Eq. (10), is presented in Fig. 4(a). The simulated composite image generated from the point-source objective function $O_1(x)$ is presented in Fig. 4(a). As expected, the simulated PSF is equal to the product of the two-photon excitation field with the Franunhofer diffraction PSF. The MTF of two-photon SW-TIRM is presented in Fig. 4(b). The S/N distribution under uniform illumination, i.e., object function $O_3(x)$, is shown in Fig. 4(e). To fur-

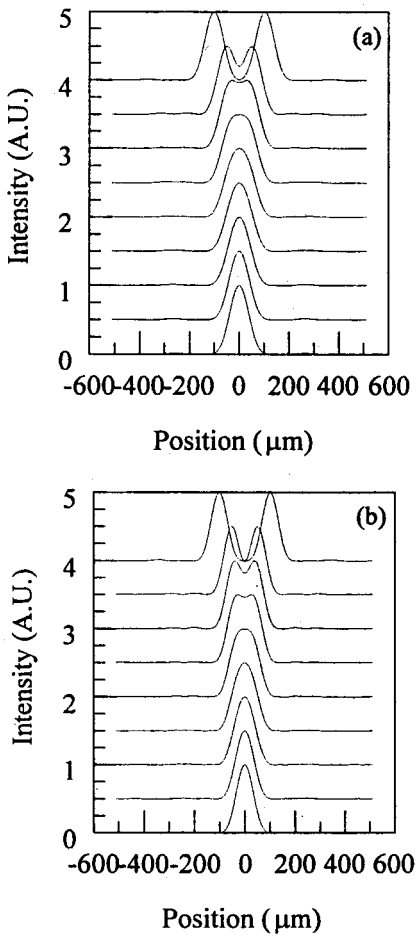

Fig. 5. (a) Simulated composite images for two-photon SW-TIRM imaging at 900-nm excitation of two point objects separated by 20, 30, 40, 50, 60, 70, 80, 100, and 200 nm. (b) Simulated composite images of two-photon SW-TIRM imaging at 750-nm excitation of two point objects separated by 20, 30, 40, 50, 60, 70, 80, 100, and 200 nm. These images are normalized and are displaced from each other vertically for the clarity of the presentation.

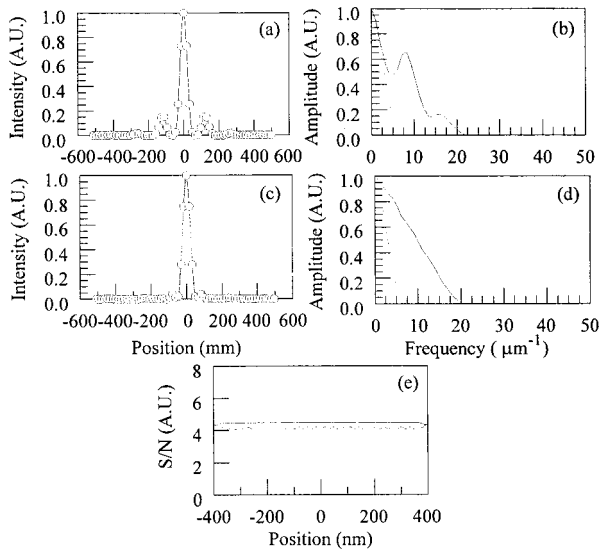

Fig. 6. (a) Theoretical PSF of pump-probe SW-TIRM in transient absorption mode as predicted by Eq. (10) (solid curves) and simulated composite image of a point source imaged by pump–probe SW-TIRM in transient absorption mode (data points). (b) MTF of pump–probe SW-TIRM in transient absorption mode (solid curves) and MTF of Fraunhofer diffraction PSF (dotted curves). (c) Theoretical PSF of pump–probe SW-TIRM in stimulated-emission mode as predicted by Eq. (10) (solid curves) and simulated composite image of a point source imaged by pump-probe SW-TIRM in stimulated-emission mode (data points). (d) MTF of pump-probe SW-TIRM in stimulated-emission mode (solid curves) and MTF of Fraunhofer diffraction PSF (dotted curve). (e) S/N distribution in pump–probe SW-TIRM images in stimulated-emission mode (upper curve) and in transient absorption mode (lower curve).

ther investigate the ability of this method to resolve closely spaced objects, we generated numerical simulated composite images with use of object functions $O_2(x)$ [Fig. 5(a)]. One concludes that two-photon excitation has lower resolution than one-photon SW-TIRM. However, the use of two-photon excitation effectively suppresses the sidebands of the PSF by over one order of magnitude. Similar results are observed in other forms of high-resolution microscopy.[13]

Since many fluorophores can be excited under two-photon mode at wavelengths substantially shorter than their twice one-photon excitation wavelengths,[30,31] simulation results by use of an excitation wavelength at 750 nm are also presented [Figs. 4(c), 4(d) and 5(b)]. In this case, the FWHM of the PSF is comparable to that of one-photon SW-TIRM but provides better sideband suppression.

C. Pump–Probe Standing-Wave Total Internal Reflection Microscopy

The use of pump-probe techniques has been shown to improve resolution in fluorescence microscopy. Pump–probe microscopy can be implemented in two ways: it can be based on transient absorption or on stimulated emission processes.[32] In the transient-absorption mode, the pump and probe beams have the same wavelengths that are equal to the one-photon excitation wavelength of the fluorophore. Each of these beams produces standing-wave excitation field of the forms

$$E_{\mathrm{pu}}(x) = 1 + \cos(Kx), \tag{40}$$

$$E_{\mathrm{pr}}(x) = 1 + \cos(Kx + \phi). \tag{41}$$

For the case $\phi = 0$, the transient absorption signal has the form

$$E_{\mathrm{pu-pr}}(x) = [1 + \cos(Kx)]^2. \tag{42}$$

It should be noted that $E_{\mathrm{pu-pr}}(x)$ is not just an excitation field, as in the SW-TIRM or in the two-photon SW-TIRM cases but is a fluorescence signal distribution created by the interaction of the pump and the probe beams. Further, the signal $E_{\mathrm{pu-pr}}(x)$ is mixed with a background fluorescence signal that must be isolated experimentally on the basis of time-resolved techniques, as previously described.[18] Nevertheless, in terms of exploiting the high-frequency content of $E_{\mathrm{pu-pr}}(x)$ for standing-wave imaging, it can be treated theoretically as any other excitation field.

Since pump–probe transient absorption has the same functional form as two-photon excitation, the algorithm represented by Eqs. (37)–(39) is also appropriate for this case. For numerical simulation, the excitation wave-

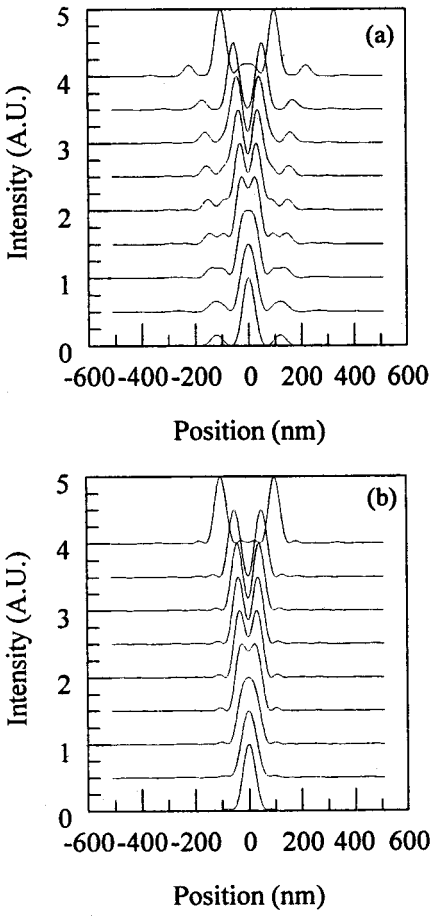

Fig. 7. (a) Simulated composite images for pump–probe SW-TIRM imaging in transient absorption mode of two point objects separated by 20, 30, 40, 50, 60, 70, 80, 100, and 200 nm. (b) Simulated composite images of pump–probe SW-TIRM imaging in stimulated-emission mode of two point objects separated by 20, 30, 40, 50, 60, 70, 80, 100, and 200 nm. These images are normalized and are displaced from each other vertically for the clarity of the presentation.

length is chosen to be 450 nm. Pump–probe SW-TIRM in transient absorption provides further resolution improvement. The simulated PSF of the composite image based on object function $O_1(x)$ is shown in Fig. 6(a), and its associated modulation transfer function is shown in Fig. 6(b). The S/N distribution on the image plane for uniform excitation, $O_3(x)$, is shown in Fig. 6(e). The composite images resulted from the object function, $O_2(x)$, at various separation parameters are shown in Fig. 7(a).

In the stimulated-emission mode, the selection of excitation and de-excitation wavelengths involves choosing a de-excitation wavelength that is far from the excitation band; this optimizes the de-excitation process and minimizes the re-excitation of the fluorophores. The application of stimulated-emission pump–probe microscopy in a standing-wave setting has an additional constraint that the excitation and emission wavelengths must be approximately integer multiple of each other; otherwise, there will be no long-range phase correlation that permits SW-TIRM imaging. Pump and probe beams with wavelengths that are exact multiples can be created by second (or third) harmonic generation.

The standing-wave field of the pump beam can be expressed as

$$E_{\mathrm{pu}}(x) = 1 + \cos(2Kx). \tag{43}$$

The standing-wave field of the probe beam with half the spatial frequency can be expressed as

$$E_{\mathrm{pr}}(x) = 1 + \cos(Kx + \phi). \tag{44}$$

In this equation, K is the wave vector of the evanescence wave generated by the probe beam. The pump–probe signal will have a spatial profile that is a product of the pump and probe beam. The most important case is for $\phi = 0$:

$$\begin{aligned} E_{\mathrm{pu-pr}}(x) &= \frac{1}{4}[1 + \cos(2Kx)][1 + \cos(Kx)] \\ &= \frac{1}{4} + \frac{3}{8}\cos(Kx) + \frac{1}{4}\cos(2Kx) \\ &\quad + \frac{1}{8}\cos(3Kx). \end{aligned} \tag{45}$$

This is an even excitation field with Fourier components $a_0 = 1/4$, $a_1 = 3/8$, $a_2 = 1/4$, and $a_3 = 1/8$. All higher-order a_n and all b_n are zero. The algorithm to apply this excitation profile for standing-wave imaging can be derived similarly. Since the highest Fourier order, m, is 3, this system will require seven shift vectors:

$$\{x'\} = \left\{0, \frac{2\pi}{7K}, -\frac{2\pi}{7K}, \frac{4\pi}{7K}, -\frac{4\pi}{7K}, \frac{6\pi}{7K}, -\frac{6\pi}{7K}\right\}, \tag{46}$$

$$\begin{aligned} f(x, x') &= A_0(x') + A_1(x')\cos Kx + A_2(x')\sin Kx \\ &\quad + A_3(x')\cos 2Kx + A_4(x')\sin 2Kx \\ &\quad + A_5(x')\cos 3Kx + A_6(x')\sin 3Kx, \end{aligned} \tag{47}$$

$$A = \begin{bmatrix} 0.143 & 0.286 & 0 & 0.286 & 0 & 0.286 & 0 \\ 0.143 & 0.178 & 0.223 & -0.064 & 0.279 & -0.257 & 0.124 \\ 0.143 & 0.178 & -0.223 & -0.064 & -0.279 & -0.257 & -0.124 \\ 0.143 & -0.064 & 0.279 & -0.257 & -0.124 & 0.178 & -0.223 \\ 0.143 & -0.064 & -0.279 & -0.257 & 0.124 & 0.178 & 0.223 \\ 0.143 & -0.257 & 0.124 & 0.178 & -0.223 & -0.064 & 0.279 \\ 0.143 & -0.257 & -0.124 & 0.178 & 0.223 & -0.064 & -0.279 \end{bmatrix}. \tag{48}$$

For the simulation of pump–probe SW-TIRM in stimulated-emission mode, the pump and probe wavelengths are 450 and 900 nm, respectively. The simulated composite image of a point source, $O_1(x)$, is shown in Fig. 6(c). The associated MTF is shown in Fig. 6(d). The S/N distribution in the composite image for uniform excitation, $O_3(x)$, is shown in Fig. 6(e). The composite images that resulted from the object function, $O_2(x)$, at various separation parameters are shown in Fig. 7(b).

4. RESOLUTION ENHANCEMENT BASED ON IMPULSE-FUNCTION DECOMPOSITION

When the excitation field cannot be expanded in terms of a few Fourier components, the computational complexity is significant for the algorithm based on Fourier decomposition. More importantly, there are situations where the exact functional form of the excitation field is unknown. An example of these difficulties arising is stimulated emission depletion (STED) SW-TIRM. In this session, we will derive an alternative algorithm based on impulse function decomposition of $f(x, x')$ that does not require an exact knowledge of the excitation field's functional form.

A. Non-periodic Excitation Field

Let $E(x)$ be the excitation field that is consistent with the previous assumptions: (1) it can be translated along the object plane and (2) it contains super-diffraction-limited frequency components. For the following discussion, we will further assume that $E(x)$ is inversion invariant, i.e.,

$$E(-x) = E(x). \tag{49}$$

With inversion symmetry, Eq. (8) can be written as

$$\sum_{\{x'\}} f(x, x')E(x' - x'') = E(x - x''). \tag{50}$$

A solution of Eq. (50) consists of a set of shift vectors that covers the whole real line,

$$\{x'\} = \Re, \tag{51}$$

and the weighting function

$$f(x, x') = \delta_{x-x'}, \tag{52}$$

where δ_x is the Kronecker delta function, where

$$\delta_x = \begin{cases} 0 & x \neq 0 \\ 1 & x = 0 \end{cases}. \tag{53}$$

To demonstrate that for this choice of $\{x'\}$ Eq. (52) is a solution of Eq. (50), we can substitute Eqs. (51) and (52) into the left-hand side of Eq. (50) and obtain

$$\sum_{\{x'\}} f(x, x')E(x' - x'') = \sum_{\{x'\}\in\Re} \delta_{x-x'}E(x' - x'') = E(x - x''). \tag{54}$$

The last equality holds, since the only nonvanishing term in the sum is $x' = x$.

Equation (5) can now be written as

$$I'(x) = \sum_{\{x'\}\in\Re} I(x, x')\delta_{x-x'}. \tag{55}$$

Note that the domain of x' is, in principle, the whole real line; however, since the Kronecker delta is zero unless $x' = x$, the only relevant subset of $\{x'\}$ consists of positions x where the final image is to be evaluated. Since the final image is evaluated only at discrete points, this allows practical implementation of this algorithm. At each position x where the final high-resolution image $I'(x)$ is to be evaluated, an intermediate image $I(x, x')$ is acquired, with the inversion center of its excitation field, x', positioned at x. The intensity of the final image at position x is equal to the intensity of this intermediate image evaluated at the same position (Fig. 10 below).

B. Periodic Excitation Field

When $E(x)$ is periodic, there can be further simplifications. Let X be the period of $E(x)$. In this case, Eq. (8) can be solved with a subset of shift vectors where

$$\{x'\} \in 0 \leqslant x' \leqslant X. \tag{56}$$

In solving Eq. (8), it is clear that $f(x, x')$ must have the same periodicity as $E(x)$. Extending Eq. (52), we have the following weighting function:

$$f(x, x') = \delta_{x-nX-x'}, \tag{57}$$

where n is the largest positive integer in which $nX \leqslant x$. One can show that Eqs. (56) and (57) are a solution of Eq. (50) by substitution:

$$\sum_{\{x'\}} f(x, x')E(x' - x'') = \sum_{0\leqslant x'\leqslant X} \delta_{x-nX-x'}E(x' - x'') = E(x - nX - x'') = E(x - x''). \tag{58}$$

The second equality is based on the fact that the only nonzero term of this sum is when $x' = x - nX$. The third inequality is based on the periodicity of $E(x)$.

For a nonperiodic excitation field, the intermediate image generated by a given shift vector x' determines the value at a single point x in the final image where $x = x'$. For the periodic excitation field, the intermediate image generated by a given shift vector x' determines the values of the composite image at multiple points x at periodic intervals where $x + nX = x'$ and $n = 0, \pm 1, \pm 2, \ldots$.

C. Stimulated Emission Depletion Standing-Wave Total Internal Reflection Microscopy

Impulse decomposition algorithm is needed in STED SW-TIRM. The concept of STED is similar to pump–probe microscopy. However, unlike pump–probe microscopy, where the signal is bilinear with the pump and probe beam intensities, the stimulated-emission beam used in STED microscopy operates in a highly nonlinear regime, resulting in a strong suppression of fluorescence in the outer region of the PSF. This results in a significant narrowing of the PSF.

It is clear that the concept of STED can be applied to SW-TIRM to provide further resolution enhancement. The basic theory of STED has been previously described.[21] Briefly, the spatial-temporal behavior of a fluorophore in the presence of pump (excitation) and probe (STED) beams can be described as

$$\begin{aligned}
\frac{dn_0}{dt} &= h_{exc}(x, t)\sigma_{01}(n_1 - n_0) + \frac{1}{\tau_{vibr}}n_3, \\
\frac{dn_1}{dt} &= h_{exc}(x, t)\sigma_{01}(n_0 - n_1) - \frac{1}{\tau_{vibr}}n_1, \\
\frac{dn_2}{dt} &= \frac{1}{\tau_{vibr}}n_1 + h_{STED}(x, t)\sigma_{23}(n_3 - n_2) - \left(\frac{1}{\tau_{fluor}} + Q\right)n_2, \\
\frac{dn_3}{dt} &= h_{STED}(x, t)\sigma_{23}(n_2 - n_3) + \left(\frac{1}{\tau_{fluor}} + Q\right)n_2 - \frac{1}{\tau_{vibr}}n_3.
\end{aligned} \tag{59}$$

In this set of differential equations, n_0, n_1, n_2, and n_3 are, respectively, the population of the lowest vibrational level in the electronic ground state, the population of an upper vibrational level in the electronic excited state, the population of the lowest vibrational level in the electronic excited state, and the population level of an upper vibrational level in the electronic ground state. The fluorescence signal detected is proportional to the population of n_2, the population of molecules undergoing spontaneous de-excitation. σ_{01} and σ_{23} are the absorption and stimulated emission cross sections of the fluorophore. τ_{fluor} and τ_{vibr} are the fluorescence lifetime and the vibrational relaxation time of the fluorophore. Q is the spontaneous quenching rate. $h_{exc}(x, t)$ and $h_{STED}(x, t)$ are the spatial temporal profiles of the excitation and the STED fields. Similar to pump–probe microscopy, the need for long-range correlation of the pump and probe fields requires that the excitation and STED wavelengths be exact mul-

tiples. We will consider the case where the STED wavelength is exactly twice that of the excitation wavelength.

The standing-wave field of the excitation beam can be expressed as

$$h_{\mathrm{exc}}(x, t) = h_{\mathrm{exc}}(t)[1 + \cos(2Kx)]. \quad (60)$$

The standing-wave field of the STED beam with half the spatial frequency can be expressed as

$$h_{\mathrm{STED}}(x, t) = h_{\mathrm{STED}}(t)[1 + \cos(Kx + \phi)]. \quad (61)$$

While the phase factor ϕ can assume different values, we will focus on the case of $\phi = \pi/2$, where the most efficient suppression of the outer region of the PSF can be achieved. In this case, Eq. (61) can be rewritten as

$$h_{\mathrm{STED}}(x, t) = h_{\mathrm{STED}}(t)[1 - \cos(Kx)]. \quad (62)$$

The set of differential equations [Eq. (59)] describing STED SW-TIRM can be solved numerically. The spatial distribution of the fluorescence signal at increasing strength of STED beam under a constant excitation beam was calculated numerically with use of a fourth-order Runge–Kutta algorithm that used realizable parameters

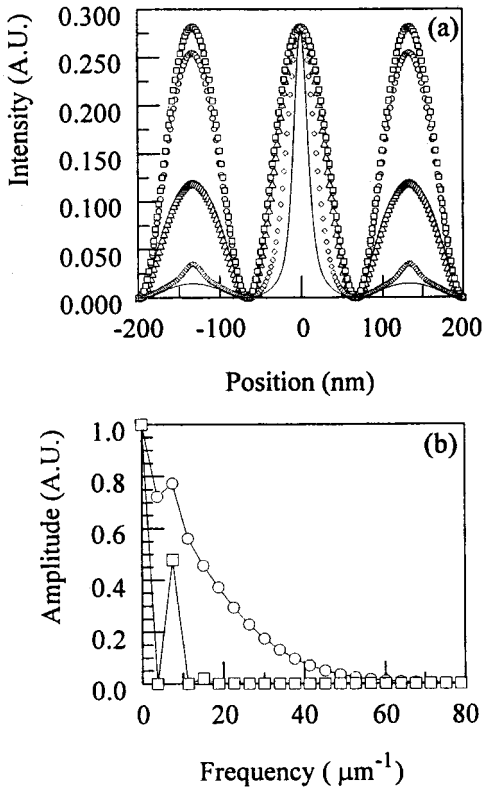

Fig. 8. (a) Fluorescence intensity distribution generated by evanescence fields in STED configuration. The parameters of this simulation are: $\sigma_{01} = \sigma_{23} = 5 \times 10^{-7}\ \mu\mathrm{m}^2$, $\tau_{\mathrm{fluor}} = 2$ ns, $\tau_{\mathrm{vibr}} = 0.002$ ns, $Q = 0.1\ \mathrm{ns}^{-1}$, $h_{\mathrm{exc}} = 2\ \mathrm{W}\,\mu\mathrm{m}^{-2}$. A range of STED beam intensity is evaluated: $h_{\mathrm{STED}} = 0\ \mathrm{W}\,\mu\mathrm{m}^{-2}$ (square), $h_{\mathrm{STED}} = 0.1\ \mathrm{W}\,\mu\mathrm{m}^{-2}$ (circle), $h_{\mathrm{STED}} = 1\ \mathrm{W}\,\mu\mathrm{m}^{-2}$ (triangle), $h_{\mathrm{STED}} = 10\ \mathrm{W}\,\mu\mathrm{m}^{-2}$ (diamond), $h_{\mathrm{STED}} = 50\ \mathrm{W}\,\mu\mathrm{m}^{-2}$ (solid curve). Other parameters used in the simulation are specified in Section 3.B; in particular, the wavelength of the excitation beam is set at 450 nm, and the wavelength of the STED beam is set at 900 nm. (b) Fourier transform of fluorescence intensity distribution generated by evanescence fields in STED configuration with STED beam intensities of 50 $\mathrm{W}\,\mu\mathrm{m}^{-2}$ (circles) and 0 $\mathrm{W}\,\mu\mathrm{m}^{-2}$ (squares).

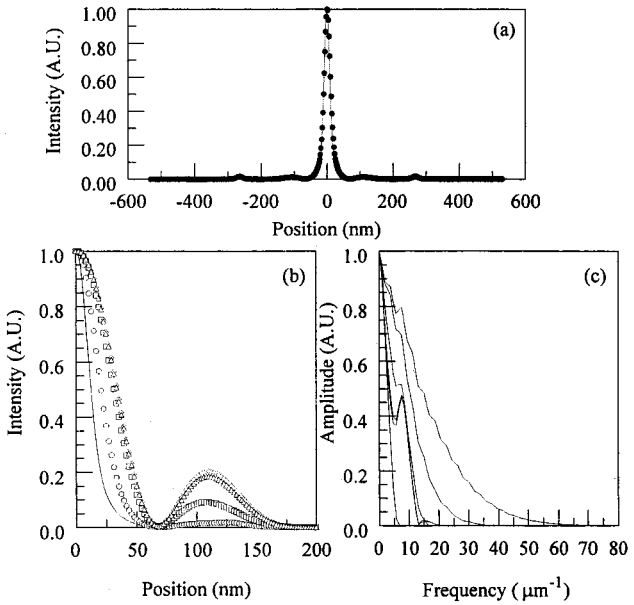

Fig. 9. (a) Theoretical PSF of STED SW-TIRM imaged with use of 50 $\mathrm{W}\,\mu\mathrm{m}^{-2}$ STED beam intensity as predicted by Eq. (10) (solid curves) and simulated composite image of a point source imaged by STED SW-TIRM with use of 50 $\mathrm{W}\,\mu\mathrm{m}^{-2}$ STED beam (data points). (b) Simulated PSFs of STED SW-TIRM imaged with use of 50 $\mathrm{W}\,\mu\mathrm{m}^{-2}$ STED beam intensity (solid curves), 10 $\mathrm{W}\,\mu\mathrm{m}^{-2}$ STED beam intensity (circles), 1 $\mathrm{W}\,\mu\mathrm{m}^{-2}$ STED beam intensity (squares), 0.1 $\mathrm{W}\,\mu\mathrm{m}^{-2}$ STED beam intensity (triangles), and 0 $\mathrm{W}\,\mu\mathrm{m}^{-2}$ STED beam intensity (diamonds). (c) MTFs of STED SW-TIRM PSFs with STED beam intensity set to 50 $\mathrm{W}\,\mu\mathrm{m}^{-2}$, 10 $\mathrm{W}\,\mu\mathrm{m}^{-2}$, 1 $\mathrm{W}\,\mu\mathrm{m}^{-2}$, 0.1 $\mathrm{W}\,\mu\mathrm{m}^{-2}$, and 0 $\mathrm{W}\,\mu\mathrm{m}^{-2}$ (from right to left).

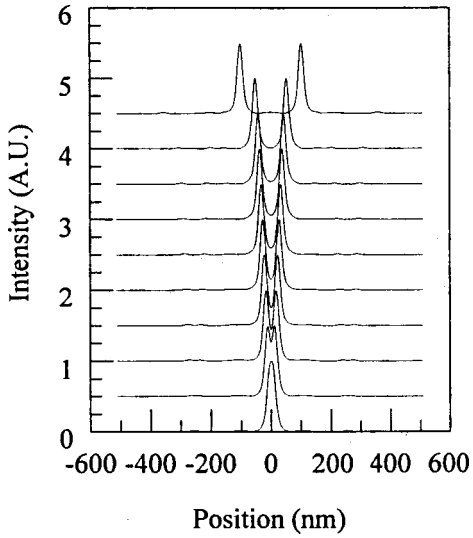

Fig. 10. Simulated composite images for STED SW-TIRM imaging with 50 $\mathrm{W}\,\mu\mathrm{m}^{-2}$ STED beam intensity of two point objects separated by 10, 20, 30, 40, 50, 60, 70, 80, 100, and 200 nm. These images are normalized and are displaced from each other vertically for the clarity of the presentation.

[Fig. 8(a)].[33] The number of Fourier components required to describe the STED excitation field can be calculated from the Fourier transform of these fluorescence distributions. The Fourier transforms at the highest and lowest STED beam intensities are shown [Fig. 8(b)]. This shows that the highly nonlinear nature of the exci-

tation profile under high-intensity STED beams cannot be adequately approximated by a few Fourier components. This large number of nonzero components makes the application of Fourier decomposition algorithm computationally cumbersome. More importantly, a large number of experimental parameters such as the excitation cross section, the stimulated emission cross section, and the fluorescence lifetime, either are not precisely known or are sensitive to specimen chemical environment. The exact fluorescence profile is further highly dependent upon STED beam intensity [Fig. 8(a)]. Therefore the fluorescence profile in the STED case cannot be quantified *a priori* in practice. This is very different from the case of SW-TIRM, where the excitation profile is very close to theoretical prediction as long as there is no excitation saturation. Clearly, impulse function decomposition approach is more appropriate for the STED SW-TIRM case. The accuracy of this algorithm to produce the expected PSF is tested by simulation. The simulated result generated by imaging a point object $O_1(x)$ is presented in Fig. 9(a). This result is in good agreement with the expected PSF, which is equal to the product of the calculated fluorescence distribution [Fig. 8(a)] with the Fraunhofer PSF. The composite images of a point source imaged with use of STED SW-TIRM at different STED beam intensities are shown in Fig. 9(b). The corresponding MTFs are shown in Fig. 9(c). The ability of this technique to resolve two closely spaced point objects, $O_2(x)$, is shown in Fig. 10. The incorporation of STED method is very promising and allows significant resolution enhancement of standard SW-TIRM by almost another factor of two to three. This method allows point objects to be resolved that are separated by as little as 30 nm, corresponding to about $\lambda_e/20$.

5. CONCLUSIONS

Standing-wave microscopy belongs to a class of imaging technique where super-diffraction limited images can be generated. The origin of this ability to produce very-high-resolution images lies in the presence of an excitation field that contains super-diffraction-limited frequency components. While the fluorescence generated at the object planes contains high-frequency information of the object distribution, this information is lost at the image plane where the detection optics act as a low-pass filter. In this report, we have shown if this excitation field can be translated spatially, the high-frequency information encoded in the intensity distribution of the image can be extracted from a set of intermediate images where the origins of the excitation fields are translated to different locations. Further, the properties of the detection optics, such as the objective, play a relatively minor role in setting resolution limits. Two algorithms are developed to combine this set of images into a high-resolution composite image. One of these algorithms, based on Fourier decomposition, requires knowledge of the exact functional form of the excitation field, while the other algorithm based on impulse function decomposition requires only that the excitation field have inversion symmetry. We should stress that these algorithms developed are general methods in PSF engineering and are not specific to the SW-TIRM case. They are applicable to any situation where a translatable, high-frequency excitation field is present.

Since these algorithms are general, they allow easy evaluation of the potential of incorporating a variety of nonlinear excitation techniques to improve the resolution of SW-TIRM. The nonlinear excitation techniques evaluated include two-photon, pump–probe and STED methods. The potential of these methods for super-diffraction-limited imaging has been studied by use of numerical simulation. The simulation results are summarized in Table 1. We found that the use of two-photon excitation produces PSF with FWHM that is wider or comparable to SW-TIRM. However, this excitation does provide better suppression of the sidebands of the PSF. This is particularly important when objective lenses with lower numerical aperture are used. Pump–probe microscopy is another valuable addition to SW-TIRM. Operating in either transient absorption or stimulated emission mode, pump–probe SW-TIRM provides higher resolution than

Table 1. Characteristics of PSFs and MTFs of Fluorescence Microscopy (FM), SW-TIRM, Two-Photon SW-TIRM (2p SW-TIRM), Pump–Probe SW-TIRM (pp SW-TIRM), and STED SW-TIRM

Methods	FWHM of PSF (nm)	First sideband Location (nm)	Amplitude Ratio[a]	Maximum Frequency of MTF[b] (μm^{-1})
FM	162	260	0.02	6
SW-TIRM	60	112	0.18	14
2p SW-TIRM (λ_{exc} = 900 nm)	80	265	0.02	13
2p SW-TIRM (λ_{exc} = 750 nm)	68	163[c]	0.004	15
pp SW-TIRM (transient absorption)	44	120	0.15	22
pp SW-TIRM (stimulated emission)	48	79	0.04	20
STED SW-TIRM (h_{STED} = 50 W/μm^{-2})	21	108	0.01	56

[a] Ratio of the first sideband and the main peak.
[b] Second sideband has higher amplitude in this case. It locates at 244 nm away with an amplitude ratio of 0.01.
[c] Maximum frequency of MTF is measured to be the frequency where the amplitude falls to the 1% level.

SW-TIRM. Pump–probe SW-TIRM in transient-absorption mode has slightly better resolution, but the stimulated-emission mode provides better sideband suppression. The highest resolution can be achieved with use of STED SW-TIRM. Resolving point objects with separations of less than 30 nm appears to be feasible. STED SW-TIRM also provides excellent sideband suppression. One drawback of this method is that the PSF is no longer known *a priori*, nor is it invariant in the image, since the PSF is a function of the fluorophores' photophysical properties and their local chemical environment.

ACKNOWLEDGMENT

This work is supported by National Science Foundation grants MCB-9604382 and DBI-9987122.

Corresponding author Peter T. C. So can be reached at the address on the title page or by e-mail at ptso@mit.edu.

REFERENCES

1. G. Binning, C. F. Quante, and C. Gerber, "Atomic force microscope," Phys. Rev. Lett. **12**, 930–933 (1986).
2. G. Binning and H. Rohrer, "Scanning tunneling microscopy," IBM J. Res. Dev. **30**, 355 (1986).
3. E. Betzig, J. K. Trautman, T. D. Harris, J. S. Weiner, and R. L. Kostalak, "Breaking the diffraction barrier: optical microscopy on a nanometric scale," Science **251**, 1469–1470 (1991).
4. R. C. Dunn, G. R. Holtom, L. Mets, and X. S. Xie, "Near-field fluorescence imaging and fluorescence lifetime measurement of light harvesting complexes in intact photosynthetic membranes," J. Phys. Chem. **98**, 3094–3098 (1994).
5. V. Subramaniam, A. K. Kirsch, and T. M. Jovin, "Cell biological applications of scanning near-field optical microscopy (SNOM)," Cell Mol. Biol. **44**, 689–700 (1998).
6. A. K. Kirsch, V. Subramaniam, G. Striker, C. Schnetter, D. J. Arndt-Jovin, and T. M. Jovin, "Continuous wave two-photon scanning near-field optical microscopy," Biophys. J. **75**, 1513–1521 (1998).
7. T. Wilson and C. J. R. Sheppard, *Theory and Practice of Scanning Optical Microscopy* (Academic, New York, 1984).
8. T. Wilson, *Confocal Microscopy* (Academic, London, 1990).
9. J. B. Pawley, ed., *Handbook of Confocal Microscopy* (Plenum, New York, 1995).
10. B. R. Masters, *Selected Papers on Confocal Microscopy* (SPIE Press, Bellingham, 1996).
11. S. Hell and E. H. K. Stelzer, "Properties of a 4Pi confocal fluorescence microscope," J. Opt. Soc. Am. A **9**, 2159–2166 (1992).
12. S. Hell, W. S. Lindek, and E. H. K. Stelzer, "Enhancing the axial resolution in far-field light microscopy: two-photon 4Pi confocal fluorescence microscopy," J. Mod. Opt. **41**, 675–681 (1994).
13. P. E. Haenninen, S. W. Hell, J. Salo, and E. Soini, "Two-photon excitation 4Pi confocal microscope: enhanced axial resolution microscope for biological research," Appl. Phys. Lett. **66**, 1698 (1995).
14. M. Schrader, M. Kozubek, S. W. Hell, and T. Wilson, "Optical transfer functions of 4Pi confocal microscopes: theory and experiment," Opt. Lett. **22**, 436–438 (1997).
15. W. Denk, J. H. Strickler, and W. W. Webb, "Two-photon laser scanning fluorescence microscopy," Science **248**, 73–76 (1990).
16. W. J. Denk, D. W. Piston, and W. W. Webb, "Two-photon molecular excitation laser-scanning microscopy," in *Handbook of Biological Confocal Microscopy*, J. B. Pawley, ed. (Plenum, New York, 1995), pp. 445–458.
17. P. T. C. So, C. Y. Dong, B. R. Masters, and K. M. Berland, "Two-photon excitation fluorescence microscopy," Annu. Rev. Biomed. Eng. **2**, 399–429 (2000).
18. C. Y. Dong, P. T. So, T. French, and E. Gratton, "Fluorescence lifetime imaging by asynchronous pump-probe microscopy," Biophys. J. **69**, 2234–2242 (1995).
19. C. Y. Dong, P. T. C. So, Ch. Buehler, and E. Gratton, "Spatial resolution in scanning pump-probe fluorescence microscopy," Optik **106**, 7–14 (1997).
20. Ch. Buehler, C. Y. Dong, P. T. C. So, T. French, and E. Gratton, "Time-resolved polarization imaging by pump-probe (stimulated emission) fluorescence microscopy," Biophys. J. **79**, 536–549 (2000).
21. S. W. Hell and J. Wichmann, "Breaking the diffraction resolution limit by stimulated emission: stimulated-emission-depletion fluorescence microscopy," Opt. Lett. **19**, 780–782 (1994).
22. T. A. Klar and S. W. Hell, "Subdiffraction resolution in far-field fluorescence microscopy," Opt. Lett. **24**, 954–956 (1999).
23. M. Dyba, T. A. Klar, S. Jakobs, and S. W. Hell, "Ultrafast dynamics microscopy," Appl. Phys. Lett. **77**, 597–599 (2000).
24. G. Cragg and P. T. C. So, "Standing-wave total internal reflection microscopy," Opt. Lett. **25**, 46–48 (2000).
25. J. T. Frohn, H. F. Knapp, and A. Stemmer, "True optical resolution beyond the Rayleigh limit achieved by standing wave illumination," Proc. Natl. Acad. Sci. USA **97**, 7232–7236 (2000).
26. B. Bailey, D. L. Farkas, D. L. Taylor, and F. Lanni, "Enhancement of axial resolution in fluorescence microscopy by standing-wave excitation," Nature **366**, 44–48 (1993).
27. V. Krishnamurthi, B. Bailey, and F. Lanni, "Imaging processing in 3-D standing-wave fluroescence microscopy," in *Three-Dimensional Microscopy: Image Acquisition and Processing III*, C. J. Cogswell, G. Kino, and T. Wilson, eds., Proc. SPIE **2655**, 18–25 (1996).
28. G. E. Cragg and P. T. C. So, "Standing wave total internal reflection microscopy—breaking the diffraction resolution limit," Biophys. J. **78**, 248a (2000).
29. P. R. Bevington and D. K. Robinson, *Data Reduction and Error Analysis for the Physical Sciences* (McGraw-Hill, New York, 1991).
30. C. Xu, J. Guild, W. W. Webb, and W. Denk, "Determination of absolute two-photon excitation cross sections by *in situ* second-order autocorrelation," Opt. Lett. **20**, 2372–2374 (1995).
31. C. Xu, W. Zipfel, J. B. Shear, R. M. Williams, and W. W. Webb, "Multiphoton fluorescence excitation: new spectral windows for biological nonlinear microscopy," Proc. Natl. Acad. Sci. USA **93**, 10763–10768 (1996).
32. P. T. C. So, C. Y. Dong, K. M. Berland, T. French, and E. Gratton, "Time-resolved stimulated-emission and absorption microscopy," in *Topics in Fluorescence V*, J. R. Lakowicz, ed., (Plenum, New York, 1998), 427–469.
33. W. H. Press, S. A. Teukolsky, W. T. Vetterling, and B. R. Flannery, *Numerical Recipes in C* (Cambridge U. Press, Cambridge, UK 1992).